Article

Pulsed Electro Decoration of Carbon Nanotubes with $Fe_xZn_{1-x}S$

Andjelika Bjelajac [1,2,*], **Ileana Florea** [1,3] , **Mihai Zamfir** [1,4], **Sandrine Tusseau-Nenez** [5]
and Costel Sorin Cojocaru [1]

1   LPICM, CNRS, Ecole Polytechnique, IP Paris, 91228 Palaiseau Cedex, France
2   Luxembourg Institute of Science and Technology (LIST), Maison des Matériaux, 28,
     Avenue des Hauts-Fourneaux, L-4365 Esch-sur-Alzette, Luxembourg
3   Université Côte d'Azur, CNRS, CRHEA, rue Bernard Grégory, 06560 Valbonne, France
4   National Institute for Laser, Plasma & Radiation Physics (INFLPR), Atomistilor Street, No. 409,
     RO-077125 Magurele, Ilfov, Romania
5   LPMC, CNRS, Ecole Polytechnique, IP Paris, 91228 Palaiseau Cedex, France
*   Correspondence: andjelika.bjelajac@gmail.com

Abstract: A wide ranging scientific interest in developing new and simple preparation methods for highly catalytic bimetallic sulfides provided our motivation to explore the possibility of using the pulsed electrodeposition technique for the decoration of a carbon nanotubes forest. The carbon nanotubes were obtained using the hot-filament chemical vapor deposition technique. A non-thermal plasma treatment enabled the controlled creation of defects on the carbon nanotubes' surface. These defects served as anchoring sites for the subsequent deposition of Fe and Zn nanoparticles using the pulsed electrodeposition technique. Our findings showed that only in the case of Fe deposition prior to Zn provided the formation of FeZn bimetallic-based nanoparticles, with Zn present mainly on the outer surface of the Fe core. To induce sulfurization, a thermal treatment in sulfur vapor was conducted at 500 °C, and the obtained heterostructure consisted of $Fe_{0.3}Zn_{0.7}S$ as the main phase, with the minor presence of ZnS and S residues, which was deduced from the XRD results. This study provides thorough imaging of the process, presenting for each preparation step SEM/HR-TEM findings, coupled with EDS chemical analyses. The samples were tested for photocatalytic degradation of methyl blue dye to demonstrate the photoactive behavior of the heterostructure.

Keywords: heterostructures; carbon nanotubes; photocatalysis; electron microscopy; electrodeposition

1. Introduction

In recent decades the development of binary chalcogenides, like sulfides, has drawn the focus of the scientific community due to their wide prospective use, i.e., in solar cells [1,2], batteries [3,4], and photocatalysis [5,6]. Among many non-precious transition metal sulfides, such as FeS_2 and ZnS, are seen as advantageous due to their low price, earth-abundance, and non-toxicity [7]. To overcome the drawbacks of single metal sulfides, such as in the case of FeS_2, the short carrier lifetime [8], or for ZnS, the wide bandgap energy of ~3.7 eV [9], materials engineering to create binary structures is proposed as a potential solution [5]. Fe^{2+} and Zn^{2+} ions have a similar ionic structure and a small fraction of Fe^{2+} can enter the crystal lattice of ZnS to form a new compound, ZnFeS [10]. The addition of Fe regulates the energy band structure of ZnS, makes the absorption edge redshifted, and effectively improves the photocatalytic performance. Moreover, ZnFeS has a good stability. All these merits make it an ideal photocatalytic material and superior to TiO_2, which is commonly used [11].

To improve its functional characteristics, binary sulfides are coupled with graphene [2], or its derivatives, like carbon nanotubes. When supported on graphitic materials, the conductivity for electron capture and electron transport is increased. Herein, we investigate the sequential pulsed electrodeposition (PED) technique for the deposition of Fe and Zn,

followed by thermal treatment in sulfur vapor to obtain a controllable ratio of Fe:Zn in FeZnS. The aim is to explore the synthesis parameters and their effect on the morphology and composition of the FeZn deposits. Finally, the photocatalytic activity will be assessed through the degradation of an organic pollutant in water. Kamazani et al. reported the enhancement of the photocatalytic performance of FeS_2 when doped with Zn and coupled with CNTs [12]. However, they used suspended CNTs and Zn-FeS_2@CNTs in a powder form. The use of thin porous films, such as decorated CNT carpets, supported on a substrate is advantageous as there is no need for a recovery step during the sampling process and it avoids the potentially harmful handling of the samples in nanopowder form [13]. Unlike other reported techniques for FeZnS synthesis, where very high temperatures are needed (i.e., co-precipitation with 165 h of annealing at 850 °C [14] and physical vapor deposition (PVD) under UHV [10]) and multiple steps (i.e., dry and hydrothermal [15]), the proposed PED technique, with sulfurization under S vapor, is less complex and requires less energy. Moreover, our study provides detailed insights into the chemical and morphological changes via SEM, TEM, and EDS analyses, for every preparation step, whereas others investigated only the optical properties and phase composition.

2. Experimental Part

2.1. CNT Forest Preparation

Carbon nanotubes, aligned vertically to the Al substrate, were grown as a dense forest, according to a well-established procedure already reported elsewhere [16]. In short, a molecular beam evaporation system was used for the deposition of 30 nm of an Al_2O_3 buffer layer, followed by a 5 nm Fe layer. Prior to the deposition, the substrate was heated at 300 °C to ensure better adhesion of the deposit to the substrate, and the same temperature was maintained during the double-layer deposition process. The growth of CNTs was enabled by catalytic Fe NPs, obtained through the reductive pre-treatment of an Fe thin film/Al_2O_3/Al under activated hydrogen, using a homemade double hot filament chemical vapor deposition (d-HFCVD) reactor [17]. Methane (CH_4) was used as the carbon source for the CNTs formation, introduced at a 50 standard cubic centimeters per minute (sccm) flow rate, together with a hydrogen flow of 20 sccm. The power of the two filaments for the CH_4 was set to 450 W, whereas for the H_2 filaments it was 550 W. The overall pressure was maintained at 12 mbar. These growth conditions were maintained for 30 min, after which the chamber was evacuated and the samples removed from the hot zone [18].

After the growth of the CNTs, using a homemade DC plasma-enhanced chemical vapor deposition reactor (PECVD) system [19], the samples were exposed to low-pressure non-thermal water vapor diffusive plasma, in order to induce an excessive amount of point defects in the CNTs outer wall structure. Indeed, hydrogen treatment during the CNTs growth ensured the continuous catalytic activity of Fe, but also hydrogen induced the formation of stable C–H bonds, thus passivating the CNT surface [20]. It is well known that plasma generates high-energy reactive species (electrons, ions, radicals), which can deform (O_2 plasma) and even destroy (Ar plasma) the structure of CNTs [21]. Hussain et al. [22] applied water plasma to functionalize CNTs with different oxygen groups (e.g., carboxyl, hydroxyl, and carbonyl). Therefore, we applied the post-plasma treatment in water vapor to introduce defects in the surface of the CNTs, enabling the anchoring of pulsed electro-deposited Fe/Zn particles [16]. Furthermore, with an oxygen-rich plasma treatment, the conductivity of CNTs can be increased and the carrier transport activation energy decreased [20]. Thus, H_2O plasma post-treatment is expected to provide benefits to the photocatalytic CNTs-based heterostructures in two aspects: (i) introduction of defects to the surface of CNTs and (ii) CNTs conductivity increase.

2.2. Pulsed Electrodeposition of Fe/Zn and Sulfurization

The decoration of CNTs sidewalls was conducted via the pulsed electrodeposition (PED) process, using a three-electrode setup, with a Ag/AgCl electrode as the reference electrode, the CNTs sample as the working electrode, and a graphite counter electrode.

The setup used a Bio-Logic potentiostat to supply the power, with EC-Lab software (https: //www.biologic.net/) used to set the electrodeposition parameters and design the shape of the pulses applied to the working electrode. Herein, we study the PED of Fe and subsequent PED of Zn. As it is known that the presence of Zn(II) inhibits Fe electrodeposition [23], we decided to introduce Fe first and then Zn. In reverse, prior PED of Zn would cause the formation of Zn hydroxide and the surface would be passivated, and the attachment of Fe would be unattainable. The electrodeposition process was performed in a Watts bath solution, consisting of a mixture of 139.01 g L^{-1} $FeSO_4·7H_2O$, 30 g L^{-1} H_3BO_3, and 0.5 g L^{-1} ascorbic acid ($C_6H_8O_6$) aqueous solution for the Fe nanoparticle deposition; whereas, for the subsequent deposition of Zn, a solution of 143.78 g of L^{-1} $ZnSO_4·7H_2O$, 30 g L^{-1} H_3BO_3, and 0.5 g L^{-1} $C_6H_8O_6$ was used. The acids were added in order to buffer the electrolyte acidity, so as to not damage the aluminum substrate, nor the aluminum oxide layer. Both for the Fe and, subsequently, for the Zn electrodeposition, pulses of 40 ms, with a potential amplitude of −6.5 V, followed by 110 ms resting time, using an open voltage circuit, were applied. The number of pulses for both Fe and Zn was set at 300 each. A more detailed description of the electrodeposition technique is reported elsewhere [24]. The PED parameters were chosen according to the reported values published elsewhere, aiming to achieve the dispersed deposition of the nanoparticles in order to easily follow their chemical and morphological changes during the preparation process. The rate of electrodeposition increases with the increasing frequency of the pulsation [25]; thus, we chose a duty cycle of 25% ($t_{on}/(t_{on} + t_{off})$) to avoid the agglomeration of the NPs, and also to ensure the size of NPs was ~100 nm [26], so the analyses were more accurate. In the case of smaller NPs, other phenomena might take place, like the quantum effect [27], which can cause misleading interpretations in regard to the results. After the PED, the FeZn@CNT samples were annealed in S vapor to obtain $Fe_xZn_{1-x}S$. The heating regime was 10 °C/min up to 550 °C for 30 min, at 3 mbar.

2.3. Characterization Techniques

Scanning electron microscopy (SEM) was carried out using a Hitachi S-4800 microscope at 10 kV, with the energy-dispersive X-ray spectroscopy (EDS) analyses conducted at 20 kV.

Transmission electron microscopy (TEM) was employed for the morphological and structural analyses, using a ThermoFisher (Waltham, MA, USA) Titan Themis operating at 300 kV. Prior to the analysis, the surface of the samples was scratched using a diamond scriber, so that fragments were collected on a carbon grid. To preserve the as-synthetized morphology of each analyzed sample, no solvent was used in the preparations. The EDS chemical analyses were performed in the high-angle annular dark-field scanning transmission imaging mode (HAADF-STEM), using an X-Max Oxford detector, while setting the experimental conditions so that the total current within the probe was about 85 pA. A camera length of 110 mm was chosen for recording. For the EDS analyses, the characteristic Kα X-ray energies for carbon, oxygen, zinc, iron, and sulfur were selected: 0.277 keV, 0.523 keV, 8.639 keV, 6.398 keV, and 2.308 keV, respectively.

The grazing incidence X-ray diffraction (GIXRD) measurements were carried out using a high-resolution diffractometer (SmartLab, Rigaku, Tokyo, Japan), equipped with a high-flux 9 kW rotating anode (copper source), a CBO unit, and a HyPix-3000 high energy resolution semiconductor detector. The GIXRD experimental conditions were detailed in our previous study [13].

The diffuse reflectance spectra (DRS) were recorded by a PerkinElmer Lambda 950 nm UV–Vis–NIR spectrophotometer.

2.4. Photocatalytic Measurements

The photocatalytic activity of the samples was evaluated in regard to the photodegradation of methyl blue (MB) dye, by measuring the absorbance of the MB solution at 662 nm, which can be correlated with the concentration of MB in the solution. For this purpose, a Varian Cary® 50 UV–Vis spectrophotometer was used. Specifically, 50 mL of MB solution,

with a starting concentration c_0 = 20 mg L^{-1}, was prepared, and the photodegradation was monitored with and without the catalyst involved. The first sampling was performed after 30 min in the dark, to investigate the change in the concentration due to simple adsorption. The sampling of the irradiated dye was done after 30 min, 2 h, and 6 h, followed by measuring the MB concentration, c. A Xe lamp, operating at 50 W, was put at 30 cm distance from the MB solution. The linear fitting of $\ln(c_0/c_i)$ = kt was made to approximate the kinetic rate, k [16]. To be able to compare the effectiveness of the catalyst, all the films were cut to have a 2 cm × 1 cm geometric surface.

3. Results and Discussion

Figure 1a presents a lateral view of the CNT carpet before the PED. The CNTs were ~35 μm long and ~5 nm thick. To demonstrate the effect of the plasma treatment, Raman analyses were performed, and the obtained spectra are given in Figure 1b. As the Raman D band intensity represents the existence of defects and other disorder-induced effects for any type of carbon, the higher intensity of the D band for the plasma-treated CNTs is confirmation of plasma-induced defects. Moreover, the I_D/I_G value increases from 1.17 for the as-synthesized CNTs to 1.41, due to the plasma treatment. Similar values were reported by A. Hawsawi et al., who used a similar exposure time and temperature for the water vapor plasma treatment of vertically aligned CNTs, for the subsequent deposition of W and SiO_2 particles to improve their field emission characteristics [28]. Herein, the plasma-induced defects acted as anchoring sites for the next PED. Figure 1c shows the SEM micrograph after the PED of Fe, and Figure 1d, after the PED of Fe and the subsequent PED of Zn. The decoration of CNTs with Fe and FeZn NPs was optimized in order to avoid excessive agglomeration, as the role of CNTs is to provide a high surface area for the deposited NPs. What is more, the aim of this study was to investigate the influence of the synthesis parameters on the morphology and the composition of the NPs; thus, we aimed for the NPs to be well dispersed and easily distinguished. The PED of Fe resulted in the formation of ~80 nm quasi cubic NPs, with certain agglomerations present. The post-deposition of Zn caused an increase in the size of the NPs to ~100 nm, with an irregular shape. The presence of Zn was confirmed with EDS analysis (Table 1). The spectra are provided in the Supplementary File, Figure S1.

Table 1. EDS results conducted on 1 × 1 μm^2 areas.

Sample/Element, at.%	C K	O K	Al K	Fe K	Zn K	S	Total
After PED of Fe	17.80 +/- 2.33	21.26 +/- 2.51	23.80 +/- 0.78	37.15 +/- 2.15	0.00	0.00	100.00
After PED of Fe/Zn	31.97 +/- 1.61	17.06 +/- 1.56	24.74 +/- 0.46	15.44 +/- 0.76	10.79 +/- 1.10	0.00	100.00
After sulfurization	37.04 +/- 3.05	3.19 +/- 1.49	43.40 +/- 0.82	3.19 +/- 0.57	4.20 +/- 1.15	8.97 +/- 0.42	100.00

The overall composition of FeZn@CNTs film was provided by GIXRD analysis, and the results are given in Figure 2a. Apart from the strong signal of Al support, one can observe the characteristic peaks corresponding to pure Fe and Zn metallic phases individually (03-065-4899 and 00-004-0831, respectively). The calculated cell parameters were a = 2.672 Å and c = 4.955 Å for the Zn phase, and a = 2.8696 Å for the Fe phase.

To gain deeper insight into the composition of the FeZn NPs, TEM analyses were performed together with EDS chemical mapping, conducted on several fragments of the FeZn@CNTs film, collected by scratching the film's surface and dragging the TEM grid over it. A high-angle annular dark-field image (HAADF), conducted in STEM mode on a representative area of the sample, is given in Figure 2b, with the corresponding EDS overlay and chemical composition table in Figure 2c. The chemical element maps in Figure 2d describe the bimetallic NPs of the Fe core and the thin outer layer of Zn. A negligible amount of O proved that the FeZn NPs were preserved from the oxidation.
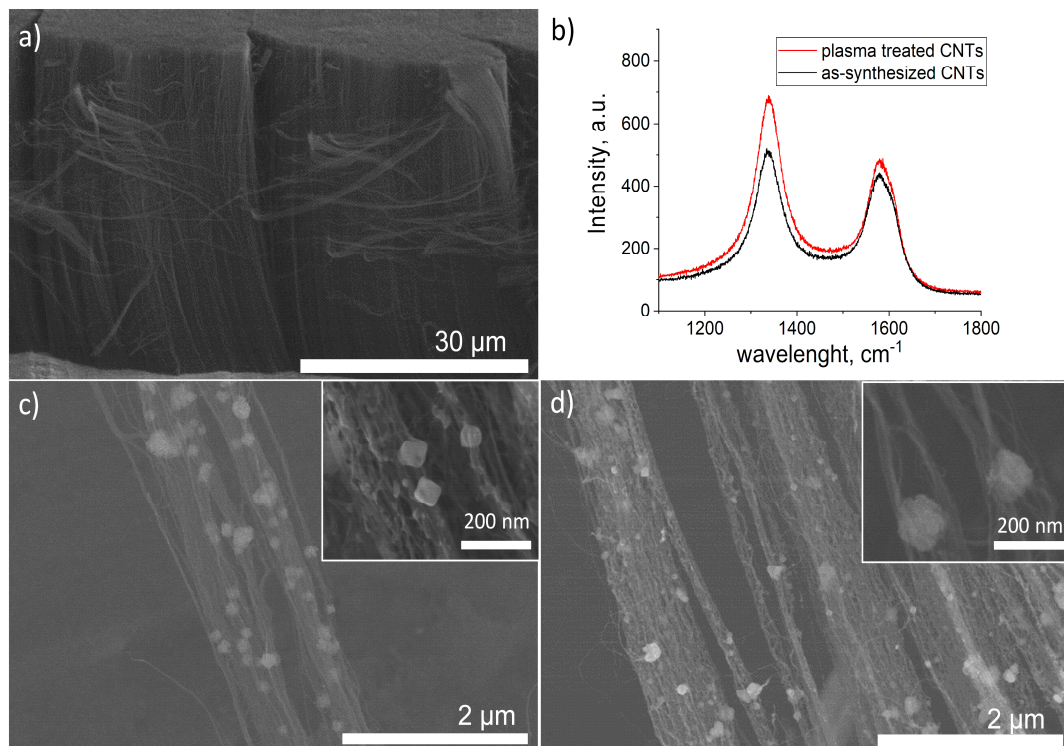
Figure 1. (**a**) SEM micrograph of as-synthesized bare CNTs, (**b**) Raman spectra of CNTs before (black) and after (red) plasma treatment, (**c**) SEM micrographs of plasma-treated CNTs after the PED of Fe, (**d**) plasma-treated CNTs after the PED of Fe and subsequent PED of Zn.
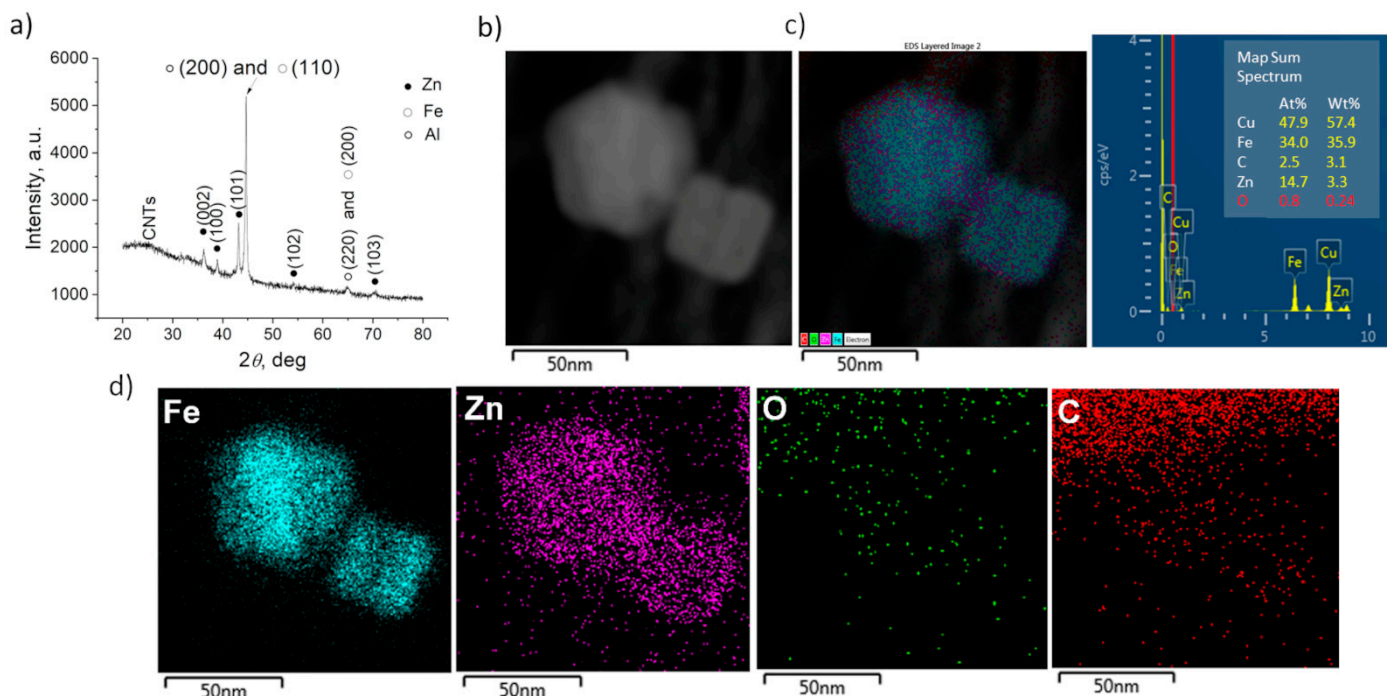

Figure 2. (**a**) GIXRD pattern of CNTs after PED of Fe/Zn and (**b**) HAADF image of a representative area of Fe/Zn@CNTs, (**c**) corresponding EDS overlay with chemical composition table, and (**d**) elemental chemical mapping of Fe, Zn, O, and C, respectively.

After the sulfurization, the same characterization approach was applied, and the representative SEM micrograph and GIXRD diffractogram are provided in Figure 3a,b, respectively. The size and shape of the NPs are not homogeneous and, according to the EDS

performed on the 1×1 μm² area (Table 1), one can assume that S was also deposited as elemental S on the surface of the CNTs, apart from being involved in $Fe_xZn_{1-x}S$ formation. The GIXRD analysis confirmed the presence of cubic $Fe_xZn_{1-x}S$, with the cell parameter calculated to be 5.4209 Å. By comparing the pattern with the data available in the PDF2 database (files 01-089-4936, 01-089-4937, 01-089-4938, 01-089-4939, 01-089-4940, 01-089-3061, and 01-089-3700), we estimated the Fe content to be $Fe_{0.289}Zn_{0.711}S$ (using Vegard's law). Based only on the work of Skinner [29] (01-089-3061), who corrected the data from Kullerud [30] (files 01-089-4936 to 4940), we calculated $Fe_{0.23}Zn_{0.77}S$. The ZnS phase (01-075-1547) and, in small amounts, FeS were also observed, as well as metallic Fe. By comparing the composition of the new FeZnS compound with the Fe/Zn ratio before sulfurization, one can assume that there is a gradient in the sulfurization impact with regards to the Zn-rich surface and Fe core. As there were also traces of ZnS and FeS detected by the XRD analysis, we assume that the sulfurization of the surface resulted in ZnS formation; whereas, on the Zn–Fe grain boundary, due to the high temperature, a mixing of Zn and Fe with diffused S resulted in the $Fe_{0.23}Zn_{0.77}S$ compound, until a certain depth toward the core where Zn did not diffuse, but only S creating FeS, leaving a certain amount of unreacted Fe. This hypothesis is based on the fact that in the alloying process, Zn interacts with Fe already at temperatures above 300 °C [31], where the diffusion of Zn is more dominant [32]. Thus, in our FeZnS interlayer, the higher amount of Zn was expected, as Zn from the surface diffused more toward the core. Figure 4 presents the STEM/EDS analysis results of the $Fe_xZn_{1-x}S$@CNTs fragment, showing that the composition of Fe:Zn:S = 14.0:20.9:25.3 (at.%).

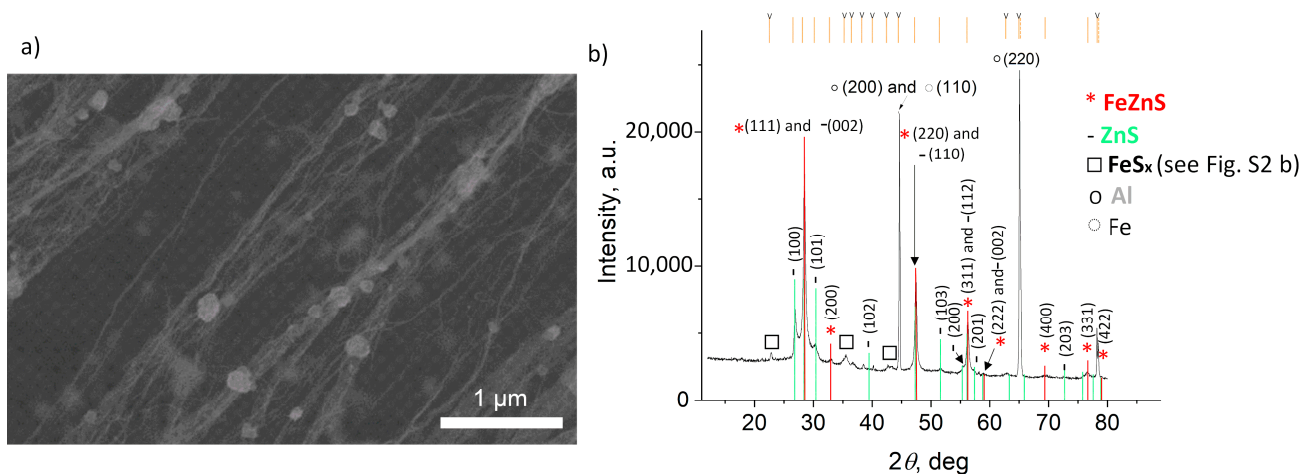**Figure 3.** (**a**) SEM micrograph and (**b**) XRD diffractogram of $Fe_xZn_{1-x}S$@CNTs.

To compare the optical properties of $Fe_xZn_{1-x}S$@CNTs with the single metal sulfide samples FeS@CNTs and ZnS@CNTs, prepared using the same synthesis conditions, the DRS spectra were recorded, and are presented in Figure 5a. In the case of ZnS@CNTs, the characteristic peak is at 363 nm, which is shifted with regards to the bare ZnS (332 nm) [33] not coupled with CNTs. A similar finding was reported by Lonkar et al., where they showed the beneficial role of graphene on the absorption properties of ZnO–ZnS heterostructures [34]. Incorporated graphene served as a macromolecular sensitizer, which caused a narrowing of the bang gap of the ZnO–ZnS heterostructures compared to the samples without graphene. The CNTs had a similar effect on FeS and $Fe_xZn_{1-x}S$, as they showed absorption along the whole visible range.
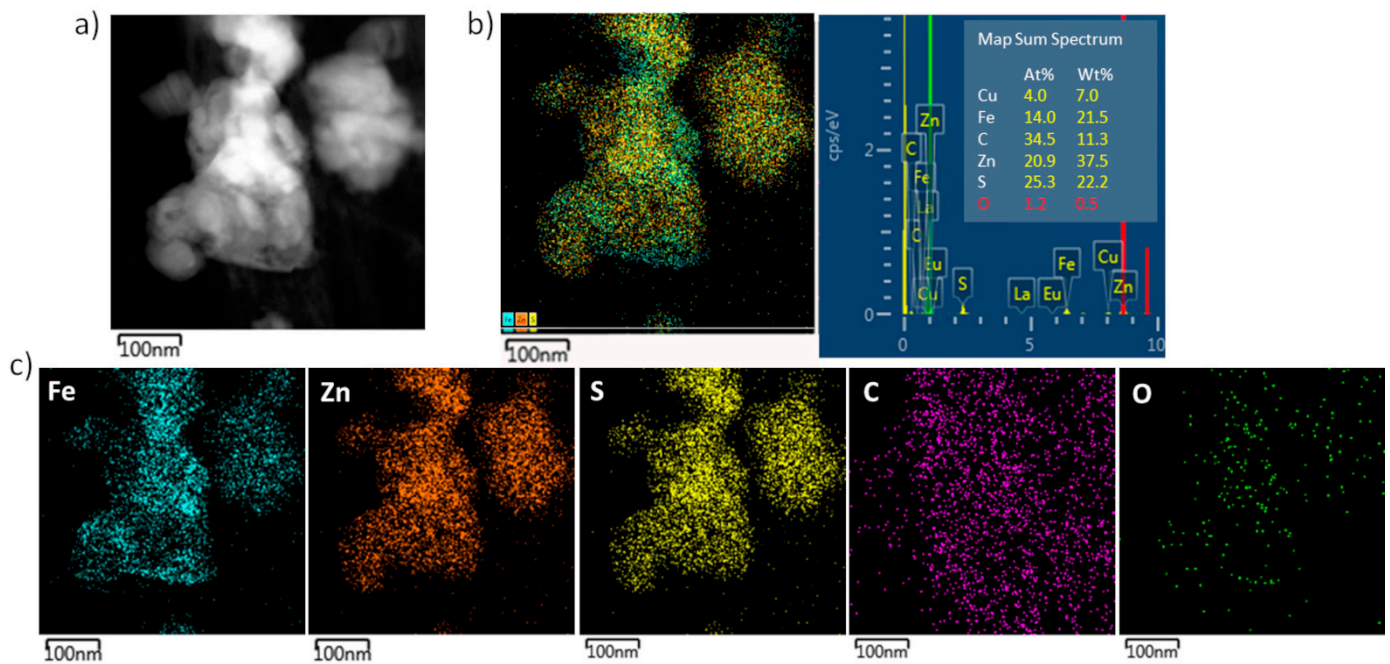
Figure 4. (**a**) HAADF image of a representative area of $Fe_xZn_{1-x}S@CNTs$, (**b**) corresponding EDS overlay, with chemical composition table, and (**c**) elemental chemical mapping of Fe, Zn, S, C, and O, respectively.
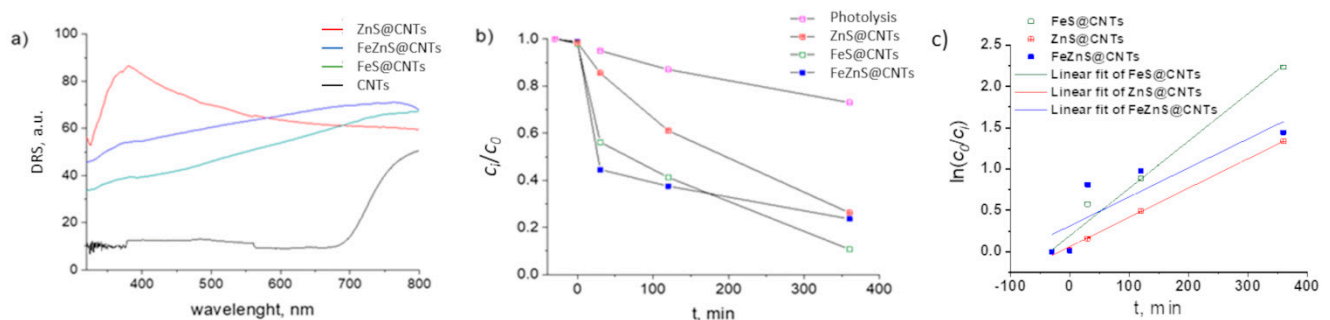

Figure 5. (**a**) DRS spectra of the analyzed samples, (**b**) photocatalytic degradation of MB dye, and (**c**) kinetic plots of MB photodegradation.

The photocatalytic measurements were performed and compared with photolysis (degradation of MB without the presence of the catalyst). The results are presented in Figure 5b. In the first 30 min, FeZnS@CNTs showed the highest photocatalytic activity (58%) with regards to ZnS@CNTs (15%) and FeS@CNTs (43%). However, it seems that its stability is an issue, as the degradation of the dye slows down and even approaches the result for ZnS@CNTs at 360 min. The kinetic constants, k, were calculated from the linear fitting of $\ln(c_0/c_i) = kt$ [35] and, indeed, FeS shows the highest value over the total duration of the photodegradation process ($k = 5.73 \times 10^{-3}$ min^{-1}), whereas FeZnS has the lowest $k = 3.17 \times 10^{-3}$ min^{-1}. The high photocatalytic efficiency of FeZnS@CNTs in the first 30 min compared to ZnS@CNTs could be due to the higher amount of photogenerated carriers originating from the absorption superiority of FeZnS. The slightly better performance of FeZnS in comparison to FeS@ZnS could be owing to the improved charge separation as we deduced earlier, namely FeZnS consists of a ZnS–FeZnS–FeS system forming a heterojunction. However, assuming the obtained multilayered system comprises of a ZnS outer layer, then a final photocatalytic performance approaching that of ZnS@CNTs is anticipated. Moreover, we assume that the FeZnS@CNT photocatalyst possesses various defects on the surface. These defects can lead to the trapping of photoelectrons and holes, which contribute to the hindering of the photocatalytic performance [6]. What is more,

photocorrosion cannot be excluded as under light illumination, metal sulfide photocatalysts generate photoelectron–hole pairs, and photogenerated holes spontaneously combine with S^{2-} to oxidize in S^0 and/or SO_4^{2-} leading to changes in the surface structure of the metal sulfide [36]. This can be avoided by the incorporation of an appropriate oxide, using the same preparation method, where instead of sulfurization, thermal annealing in an oxygen-rich atmosphere is performed [16]. However, ZnO should be avoided from the perspective of stability, as a photogenerated hole can induce the collapse of ZnO and the direct leakage of Zn^{2+} into the reaction solution [37]. In this context, we will explore further TiO_2-based heterostructures [38].

4. Conclusions

The pulsed electrodeposition technique was employed for the decoration of a CNT forest with Fe, Zn, and bimetallic core–shell FeZn. After sulfurization, the nanoparticles turned into the corresponding sulfides, with the $Fe_{0.291}Zn_{0.709}$ S composition. The contribution of the CNTs was seen to benefit to the optical properties of the sulfides. The photocatalytic activity of the films was evaluated in regard to the degradation of methyl blue dye. Even though FeZnS@CNTs showed the fastest degradation rate in the first 30 min, its stability was an issue as the degradation rate slowed down. We assume that this is due to the various defects potentially present on the surface of the FeZnS@CNTs, which act as trapping sites for the photogenerated charges. Also, the possibility of photocorrosion cannot be excluded. This could be avoided by the incorporation of an appropriate oxide, using the same preparation method, but where instead of sulfurization, thermal annealing in an oxygen-rich atmosphere is performed. This work opens up a new horizon for CNT-based heterostructure engineering, presenting a controllable method to decorate CNTs, with a photoactive core–shell structure.

References

1. Wang, M.; Qin, H.; Fang, Y.; Liu, J.; Meng, L. FeS2-sensitized ZnO/ZnS nanorod arrays for the photoanodes of quantum-dot-sensitized solar cells. *RSC Adv.* **2015**, *5*, 105324–105328. [CrossRef]
2. Yu, H.; Qian, C.; Ren, H.; Chen, M.; Tang, D.; Wu, H.; Lv, R. Enhanced catalytic properties of bimetallic sulfides with the assistance of graphene oxide for accelerating triiodide reduction in dye-sensitized solar cells. *Sol. Energy* **2020**, *207*, 1037–1044. [CrossRef]
3. Zhu, M.; Shi, J.; Xin, X.; Wu, J.; Yao, X. Bimetallic Hexagonal Layered Ni–Co Sulfides with High Electrochemical Performance for All-Solid-State Lithium Batteries. *ACS Sustain. Chem. Eng.* **2021**, *9*, 17061–17067. [CrossRef]
4. Huang, Y.; Xiong, D.; Li, X.; Sari, H.M.K.; Peng, J.; Li, Y.; Li, Y.; Li, D.; Sun, Q.; Sun, X. Recent Advances of Bimetallic Sulfide Anodes for Sodium Ion Batteries. *Front. Chem.* **2020**, *8*, 353. [CrossRef] [PubMed]

5. Li, L.; Xu, J.; Ma, J.; Liu, Z.; Li, Y. A bimetallic sulfide CuCo2S4 with good synergistic effect was constructed to drive high performance photocatalytic hydrogen evolution. *J. Colloid Interface Sci.* **2019**, *552*, 17–26. [CrossRef] [PubMed]

6. Zhang, S.; Ou, X.; Xiang, Q.; Carabineiro, S.A.; Fan, J.; Lv, K. Research progress in metal sulfides for photocatalysis: From activity to stability. *Chemosphere* **2022**, *303*, 135085. [CrossRef] [PubMed]

7. Wang, D.; Jiang, Y.; Lin, C.; Li, S.; Wang, Y.; Chen, C.; Chen, C. Solution-Processable Pyrite FeS$_2$ Nanocrystals for the Fabrication of Heterojunction Photodiodes with Visible to NIR Photodetection. *Adv. Mater.* **2012**, *24*, 3415–3420. [CrossRef] [PubMed]

8. Guo, Q.; Tang, G.; Zhu, W.; Luo, Y.; Gao, X. In situ construction of Z-scheme FeS2/Fe2O3 photocatalyst via structural transformation of pyrite for photocatalytic degradation of carbamazepine and the synergistic reduction of Cr(VI). *J. Environ. Sci.* **2021**, *101*, 351–360. [CrossRef]

9. Chang, C.-J.; Lee, Z.; Wang, C.-F. Photocatalytic hydrogen production by stainless steel@ZnS core–shell wire mesh photocatalyst from saltwater. *Int. J. Hydrogen Energy* **2014**, *39*, 20754–20763. [CrossRef]

10. Molland, N.-A.; Ghadyani, Z.; Karhu, E.A.; Poggio, S.; Nematollahi, M.; Kildemo, M.; Reenaas, T.W.; BelBruno, J.J.; Gibson, U.J. Band-edge modification and mid-infrared absorption of co-deposited Fe$_x$Zn$_{1-x}$S thin films. *Opt. Mater. Express* **2015**, *5*, 1613. [CrossRef]

11. Su, R.; Xue, Y.; Zhang, G.; Wang, Q.; Hu, L.; Wang, P. Optimization and Degradation Mechanism of Photocatalytic Removal of Bisphenol A Using Zn$_{0.9}$Fe$_{0.1}$S Synthesized by Microwave-assisted Method. *Photochem. Photobiol.* **2016**, *92*, 775–782. [CrossRef] [PubMed]

12. Kamazani, H.A.; Feizbakhsh, A.; Konoz, E.; Panahi, H.A. Zinc doped FeS$_2$/MWCNTs nanocomposites for photo-degradation application: Preparation and structural. *Mater. Res. Express* **2019**, *6*, 105092. [CrossRef]

13. Sarma, M.; Jaiswal, M.K.; Podder, S.; Bora, J.; Karmakar, S.; Choudhury, B.; Pal, A.R. A study on the applicability of thin film over powder for visible light photocatalysis. *Phys. B Condens. Matter* **2023**, *670*, 415354. [CrossRef]

14. Deulkar, S.; Bhosale, C.; Sharon, M. Optical studies on non-stiochiometric (Zn, Fe)S chalcogenide bulk pellets prepared by coprecipitation. *Mater. Chem. Phys.* **2008**, *111*, 260–264. [CrossRef]

15. Osadchii, E.G.; Gorbaty, Y.E. Raman spectra and unit cell parameters of sphalerite solid solutions (FexZn1−xS). *Geochim. Cosmochim. Acta* **2010**, *74*, 568–573. [CrossRef]

16. Bjelajac, A.; Florea, I.; Zamfir, M.; Tusseau-Nenez, S.; Cojocaru, C.S. Photocatalytic active ZnO$_{1-x}$S$_x$@CNTs heteronanostructures. *Nanotechnology* **2023**, *34*, 495704. [CrossRef] [PubMed]

17. Kim, K.-H.; Gohier, A.; Bourée, J.E.; Châtelet, M.; Cojocaru, C.-S. The role of catalytic nanoparticle pretreatment on the growth of vertically aligned carbon nanotubes by hot-filament chemical vapor deposition. *Thin Solid Films* **2015**, *575*, 84–91. [CrossRef]

18. Castan, A.; Forel, S.; Catala, L.; Florea, I.; Fossard, F.; Bouanis, F.; Andrieux-Ledier, A.; Mazerat, S.; Mallah, T.; Huc, V.; et al. New method for the growth of single-walled carbon nanotubes from bimetallic nanoalloy catalysts based on Prussian blue analog precursors. *Carbon* **2017**, *123*, 583–592. [CrossRef]

19. He, Z.; Maurice, J.-L.; Lee, C.; Gohier, A.; Pribat, D.; Legagneux, P.; Cojocaru, C. Etchant-induced shaping of nanoparticle catalysts during chemical vapour growth of carbon nanofibres. *Carbon* **2011**, *49*, 435–444. [CrossRef]

20. Lee, S.; Peng, J.-W. Effect of plasma treatment on electrical conductivity and Raman spectra of carbon nanotubes. *J. Phys. Chem. Solids* **2011**, *72*, 1101–1103. [CrossRef]

21. Liu, Y.; Liu, L.; Liu, P.; Sheng, L.; Fan, S. Plasma etching carbon nanotube arrays and the field emission properties. *Diam. Relat. Mater.* **2004**, *13*, 1609–1613. [CrossRef]

22. Hussain, S.; Amade, R.; Jover, E.; Bertran, E. Functionalization of carbon nanotubes by water plasma. *Nanotechnology* **2012**, *23*, 385604. [CrossRef] [PubMed]

23. Gomez, E.; Pelaez, Z.; Valles, E. Electrodeposition of zinc+iron alloys I. Analysis of the initial stages of the anomalous codeposition. *J. Electroanal. Chem.* **1999**, *469*, 139–149. [CrossRef]

24. Marquardt, B.; Eude, L.; Gowtham, M.; Cho, G.; Jeong, H.J.; Châtelet, M.; Cojocaru, C.S.; Kim, B.S.; Pribat, D. Density control of electrodeposited Ni nanoparticles/nanowires inside porous anodic alumina templates by an exponential anodization voltage decrease. *Nanotechnology* **2008**, *19*, 405607. [CrossRef] [PubMed]

25. Gioia, D.; Casella, I.G. Pulsed electrodeposition of palladium nano-particles on coated multi-walled carbon nanotubes/nafion composite substrates: Electrocatalytic oxidation of hydrazine and propranolol in acid conditions. *Sens. Actuators B Chem.* **2016**, *237*, 400–407. [CrossRef]

26. Aliofkhazraei, M.; Ahangarani, S.; Rouhaghdam, A.S. Effect of the duty cycle of pulsed current on nanocomposite layers formed by pulsed electrodeposition. *Rare Met.* **2010**, *29*, 209–213. [CrossRef]

27. Ghosh, C.K. Quantum Effect on Properties of Nanomaterials. In *Introduction to Nano: Basics to Nanoscience and Nanotechnology*; Sengup; Springer: Berlin/Heidelberg, Germany, 2015; pp. 73–111. [CrossRef]

28. Hawsawi, A.; Jo, S.-I.; Kang, J.S.; Park, K.-C.; Jeong, G.-H. Water vapor-induced structure modification of vertically-aligned carbon nanotube arrays and successive thin film coating for enhanced field emission properties. *Curr. Appl. Phys.* **2020**, *20*, 498–504. [CrossRef]

29. Skinner, B.J.; Barton, J.; Kullerud, G. Effect of FeS on the unit cell edge of sphalerite, a revision. *Econ. Geol.* **1959**, *54*, 1040–1046. [CrossRef]

30. Kullerud, G. The FeS-ZnS System, a geological thermometer. *Nor. Geol. Tidsskr.* **1953**, *32*, 61–147. Available online: http://books.google.ru/books?id=oM59mAEACAAJ (accessed on 1 January 2024).

31. Burton, B.P.; Perrot, P. *Phase Diagram of Binary Iron Alloys*; Okamoto, H., Ed.; American Society for Metals: Material Park, OH, USA, 1993; p. 459.
32. Shewmon, P.; Abbas, M.; Meyrick, G. Anomalously fast diffusion in the Fe-Zn System. *Met. Trans. A* **1986**, *17*, 1523–1527. [CrossRef]
33. Tang, Y.; Tian, J.; Malkoske, T.; Le, W.; Chen, B. Facile ultrasonic synthesis of novel zinc sulfide/carbon nanotube coaxial nanocables for enhanced photodegradation of methyl orange. *J. Mater. Sci.* **2017**, *52*, 1581–1589. [CrossRef]
34. Lonkar, S.P.; Pillai, V.V.; Alhassan, S.M. Facile and scalable production of heterostructured ZnS-ZnO/Graphene nano-photocatalysts for environmental remediation. *Sci. Rep.* **2018**, *8*, 13401. [CrossRef] [PubMed]
35. Guo, C.; Tao, C.; Yu, F.; Zhao, Z.; Wang, Z.; Deng, N.; Huang, X. Ball-milled layer double hydroxide as persulfate activator for efficient degradation of organic: Alkaline sites-triggered non-radical mechanism. *J. Hazard. Mater.* **2024**, *461*, 132219. [CrossRef] [PubMed]
36. Weng, B.; Qi, M.-Y.; Han, C.; Tang, Z.-R.; Xu, Y.-J. Photocorrosion Inhibition of Semiconductor-Based Photocatalysts: Basic Principle, Current Development, and Future Perspective. *ACS Catal.* **2019**, *9*, 4642–4687. [CrossRef]
37. Han, C.; Yang, M.-Q.; Weng, B.; Xu, Y.-J. Improving the photocatalytic activity and anti-photocorrosion of semiconductor ZnO by coupling with versatile carbon. *Phys. Chem. Chem. Phys.* **2014**, *16*, 16891–16903. [CrossRef]
38. Geldasa, F.T.; Kebede, M.A.; Shura, M.W.; Hone, F.G. Experimental and computational study of metal oxide nanoparticles for the photocatalytic degradation of organic pollutants: A review. *RSC Adv.* **2023**, *13*, 18404–18442. [CrossRef]